J. Fluid Mech. (1995), vol. 303, pp. 133–153

Unsteady flow about a sphere at low to moderate Reynolds number. Part 2. Accelerated motion

By EUGENE J. CHANG† AND MARTIN R. MAXEY

Center for Fluid Mechanics, Turbulence and Computation,
Brown University, Box 1966, Providence, RI 02912, USA

(Received 18 November 1994 and in revised form 6 June 1995)

A full numerical simulation based on spectral methods is used to investigate linearly accelerating and decelerating flows past a rigid sphere. Although flow separation does not occur at Reynolds numbers below 20 for a steady flow, in the linearly decelerating flow separation is observed at much lower Reynolds numbers with complete detachment of vorticity possible in certain cases. The existence of a large recirculation region contributes to the result that a negative viscous force on the sphere is possible. The contribution of the pressure to the force includes a component that is well described by the inviscid added-mass term in both the accelerating and decelerating cases. The force on the sphere is found in general to initially decay in a power law manner after acceleration or deceleration ends followed by rapid convergence at later times to the steady state. For the cases examined this convergence is found to be exponential except for those in which the sphere is brought to rest in which case the convergence remains algebraic. This includes the special case of an infinite acceleration or deceleration where the free stream velocity is impulsively changed.

1. Introduction

In part 1 of this work (Chang & Maxey 1994), referred to subsequently as Part 1, we presented results of numerical simulations for axisymmetric, oscillatory viscous flow past a rigid sphere. Structural features of the flow were identified, including the changing vorticity distribution, flow separation and the steady streaming flow induced by the oscillations at finite Reynolds numbers. Also examined were the variations in the fluid force acting on the sphere, and of special interest was an attempt at the identification of an added-mass contribution to the force. It was found that if the history force is assumed to take the same form as the classical Basset history term (Basset 1888), the added-mass effect is the same at moderate Reynolds numbers and frequencies as for both inviscid, irrotational flow (Batchelor 1967) and for unsteady Stokes flow (Basset 1888; Maxey & Riley 1983). Mei, Lawrence & Adrian (1991) obtained a similar result from their numerical study of steady flow past a sphere with a superposed oscillatory perturbation to the flow. This result is also supported by the numerical simulations of Rivero, Magnaudet & Fabre (1991). Basic questions remain though as to the exact nature of the added-mass effect in unsteady flows at finite Reynolds numbers, and how it may be affected for example by the presence of separated flow. In unsteady Stokes flow it is known that the added-mass force is

---

† Present Address: Naval Research Laboratory, Code 6410, Washington, DC 20375, USA.

affected by changes in time of a non-uniform ambient vorticity in the flow (Maxey & Riley 1993).

In order to to determine the added-mass force without making assumptions about the quasi-steady and history components of the drag we have examined flows in which a uniform free stream is linearly accelerated (or decelerated) at a constant rate from a steady state. In such a flow the added-mass effect will be immediately apparent once the acceleration has started owing to the lack of significant history and velocity-dependent effects. This approach has been used independently by Rivero *et al.* (1991) and Rivero (1991) for accelerating flows. Our results from the present study not only confirm their results for the added-mass effect but extend them to include decelerating flows, and both accelerating and decelerating flows when the acceleration is removed and the free-stream velocity assumes a new steady value. Further we demonstrate the connection between the pressure distribution and the added-mass effect at finite Reynolds numbers.

A second aim of this paper is to investigate the flow structure as it approaches a new steady state following a change in the free-stream conditions. This will give insight into the behaviour of the so-called history force which is governed by the relaxation of the flow to a steady state. The analytic results of Bentwich & Miloh (1978) and Sano (1981) state that the drag force on a sphere of radius a impulsively started from rest approaches the steady-state value at a rate proportional to $t^{-1/2}$ for small $t = O(1)$, followed by a more rapid convergence proportional to t^{-2} at large $t = O(Re^{-2})$ based on an assumption of low Reynolds numbers. Here the non-dimensional time is given as $t = t'\nu/a^2$ where ν is the kinematic viscosity. Lovalenti & Brady (1993*a*) extended this problem to include impulsive changes in velocity where the beginning and ending velocities may be other than zero and one respectively. From their analysis they found that the drag force behaved similarly for both the impulsively stopped and impulsively started sphere, the algebraic convergence at large t being due to destruction or construction of the wake region of the sphere. However, for impulsive jumps between non-zero values of the velocity, they found the convergence to be exponential at large t, this being attributed to the pre-existence of the wake region. Recently Lawrence & Mei (1995) have suggested that this latter exponential decay is only transitory for intermediate times and that in the long term the decay will be $O(t^{-2})$, dominated finally by $O(Re^2)$ contributions to the drag force neglected in Lovalenti & Brady's analysis.

A common approach to representing the fluid force on a sphere held fixed in a unidirectional, but unsteady uniform flow is to write the force F as the sum of component parts. Rivero *et al.* (1991), following earlier authors, write for example

$$F = F_S + (1 + C_M)m_F\frac{\mathrm{d}U}{\mathrm{d}t} + F_H, \tag{1.1}$$

where F_S is the quasi-steady drag force that would act on the sphere in a steady flow at the same instantaneous flow velocity $U(t)$. The second term in (1.1) combines the inertial acceleration of the uniform flow and the added-mass effect, where m_F is the mass of fluid displaced by the sphere. The third term F_H is the history term. This formulation mirrors the results obtained by Basset (1888) for low Reynolds number motion in unsteady Stokes flow, for which the added-mass coefficient $C_M = 1/2$ and the history term is

$$F_H = 6\pi a^2\mu \int_0^t \frac{\mathrm{d}U}{\mathrm{d}t'}(\pi\nu(t - t'))^{-1/2}\mathrm{d}t'. \tag{1.2}$$

Here the sphere radius is a and μ, ν are respectively the dynamic and kinematic viscosities of the fluid. This result is based on the fluid being at rest initially, at $t = 0$ (Maxey & Riley 1983). Mei & Adrian (1992) have provided an extension to this formulation (1.1) for finite Reynolds number and obtained the history term in the form

$$F_H = 6\pi a\mu \int_{-\infty}^{t} K(t-t')\frac{\mathrm{d}U}{\mathrm{d}t'}\mathrm{d}t'. \tag{1.3}$$

From previous simulation results (Mei *et al.* 1991) and asymptotic results at low Reynolds numbers they proposed a form of the history kernel $K(\tau)$ that varied as $\tau^{-1/2}$ for short times, as in Basset's result, and as τ^{-2} for longer times. This latter form would be consistent with the result of Sano (1981) for an impulsively started flow. However this form of $K(\tau)$ was obtained by extrapolating results in the frequency domain for small amplitude perturbations of a steady flow and the result has been questioned by Lovalenti & Brady (1993*b*), who present an alternative form which decays exponentially for small changes in the free-stream velocity $U(t)$. Some numerical simulations by Mei (1993), using a finite-difference scheme, do in fact show a general trend for exponential convergence to steady flow conditions in the final stage following an impulsive change in the free stream velocity. Prior to this the difference between the fluid force F and the final steady state value varies as an algebraic power in time. This conclusion though has been revised by Lawrence & Mei (1995) in light of more careful numerical simulations and theoretical arguments about the wake structure. They conclude that the convergence remains algebraic in the long term, typically as t^{-2}.

In this paper linearly accelerating and decelerating flows are studied numerically using the spectral method developed in Part 1 for the oscillating flow. We will begin by presenting the flow fields generated during and after the acceleration (or deceleration) of the free stream. The drag forces experienced by the sphere are then examined with emphasis on determining the nature of the added-mass effect. Finally, we will present results for the impulsively changed free-stream velocity in which we investigate not only the history effects on the drag force but also the evolution of the flow structure.

In the following section a short summary is given of the equations of motion and the spectral methods used to solve them for the present problem. These are the same as in Part 1, where a more complete description may be found.

2. Problem formulation

The governing equations for an incompressible viscous flow may be written in the form

$$\frac{\partial \boldsymbol{u}}{\partial t} + \boldsymbol{u}\cdot\nabla\boldsymbol{u} = -\nabla p + \frac{2}{Re}\nabla^2\boldsymbol{u} \tag{2.1}$$

$$\nabla\cdot\boldsymbol{u} = \boldsymbol{0}. \tag{2.2}$$

The free-stream velocity is parallel to and in the direction of the axis of symmetry and is given as $\boldsymbol{U} = U(t)\boldsymbol{e}^{(1)}$. All variables have been non-dimensionalized by the sphere radius a and maximum free-stream velocity $max|U(t)| = U_0$. The pressure p is scaled by ρU_0^2 where ρ is the fluid density and the Reynolds number is defined as $Re = 2aU_0/\nu$. Only linear accelerations and decelerations of the free-stream velocity are considered with

$$\left.\begin{aligned} U(t) &= c_1, & t &\leqslant t_s, \\ U(t) &= A_c(t-t_s)+c_1, & t_s &< t \leqslant t_e, \\ U(t) &= c_2, & t &> t_e, \end{aligned}\right\} \tag{2.3}$$

where c_1 and c_2 are constants such that $0 \leqslant c_i \leqslant 1$, for $i = 1,2$; t_s is the time at which an initial steady state has been reached for $U(t) = c_1$, and t_e is the time at which the acceleration is stopped. A_c is the non-dimensional acceleration of the free stream and is here called the acceleration parameter or acceleration number. It is the ratio of the scale for the temporal acceleration in the flow to the scale for the convective acceleration term in (2.1); in dimensional form the flow acceleration is $A_c U_0^2/a$. Note that for an accelerating flow $A_c > 0$ and $c_2 = 1$ and for a decelerating flow $A_c < 0$ with $c_1 = 1$.

Equations (2.1) and (2.2) are solved by introducing a scalar potential for the flow which ensures incompressibility and is of the form $\boldsymbol{u}=\nabla \times (C\boldsymbol{e}^{(\phi)})$. The pressure is eliminated by forming the equation for the vorticity $\boldsymbol{\omega}(r,\theta,t) = \nabla \times \boldsymbol{u}$, which has only one component, ω_ϕ, in an axisymmetric flow. The vorticity equation in spherical coordinates is given by

$$\frac{\partial \omega_\phi}{\partial t} = (\nabla \times \boldsymbol{u} \times \boldsymbol{\omega}) \cdot \mathbf{e}_\phi + \frac{2}{Re}\mathrm{D}^2\omega_\phi \tag{2.4}$$

where the D^2 operator is defined as $\mathrm{D}^2 = \nabla^2 - 1/(r^2 \sin^2\theta)$. The potential function C and vorticity ω_ϕ are related by

$$\mathrm{D}^2 C = -\omega_\phi. \tag{2.5}$$

Hereafter the subscript ϕ will be omitted for this vorticity component.

The boundary conditions for flow past a rigid stationary sphere held fixed at the coordinate origin are given as

$$C = 0, \ \frac{\partial C}{\partial r} = 0 \ \text{ on } \ r = 1 \tag{2.6}$$

and at large distances from the sphere

$$\omega = 0, \ C = \tfrac{1}{2}U(t) r \sin\theta \ \text{ as } \ r \uparrow \infty. \tag{2.7}$$

The potential C is written as the sum of a potential function corresponding to a prescribed flow in the free stream $\overline{C}$ and a potential corresponding to the disturbance flow produced by the presence of the sphere c: $C = \overline{C} + c$. The prescribed potential is given as $\overline{C} = \frac{1}{2}U(t) r \sin\theta$ so that ω and c vanish far from the sphere.

The non-dimensional drag force on the sphere is given as

$$C_d = F_1/\pi\rho a^2 U_0^2 \tag{2.8}$$

where F_1 is the fluid force acting on the fixed sphere in the $\boldsymbol{e}^{(1)}$ direction parallel to the free-stream velocity. Since the flow is axisymmetric, there is no lift force. The drag force C_d may be written as the sum of a frictional component due to the viscous shear stress, C_f, and a pressure component C_p. On the surface of the sphere, because of the no-slip boundary conditions, the rate of strain is equal to half the local surface vorticity and the frictional component C_f is calculated from

$$C_f = -\frac{4}{Re}\int_0^\pi \omega(r=1,\theta,t)\sin^2\theta \,\mathrm{d}\theta. \tag{2.9}$$

The pressure component C_p is calculated from the momentum equation near the surface of the sphere as noted in Part 1.

2.1. *Numerical method*

A pseudospectral or collocation method is used to represent the flow variables spatially. This is based on the formulations of Orszag (1974) and Marcus & Tuckerman (1987), and described more fully in Part 1. In brief, the vorticity ω and potential c are expanded as a Chebyshev polynomial series in the radial direction and as a sine series in the θ direction. In physical space the flow variables are represented at the collocation points

$$\theta_n = \frac{\pi n}{N+1} \text{ for } n = 1, 2, \ldots, N,$$

$$z_m = \cos^{-1}(2\pi m/M) \text{ for } m = 0, 1, \ldots, M.$$

The algebraic map $r = 1 + L(1+z)/(b-z)$ with $b = 1 + 2L/(r_\infty - 1)$ is used to map the interval $(-1, 1)$ to $(1, r_\infty)$ where r_∞ is a finite large number. The parameter L is a scaling factor used to control the spacing of the grid points.

Time integration is accomplished through an explicit second-order Adams–Bashforth scheme for the nonlinear terms and an implicit second-order Crank–Nicolson scheme for the viscous linear terms. The calculations are made in physical r-space and spectral θ-space. After discretization, equations (2.4) and (2.5) with boundary conditions (2.6) are

$$\left[1 - \frac{\Delta t}{Re}\mathrm{D}^2\right]\omega^{n+1} = \frac{\Delta t}{2}[3F^n - F^{n-1}] + \left[1 + \frac{\Delta t}{Re}\mathrm{D}^2\right]\omega^n, \tag{2.10}$$

$$\mathrm{D}^2 c^{n+1} = -\omega^{n+1}, \tag{2.11}$$

$$c^{n+1} = -\overline{C}^{n+1}, \ \frac{\partial c}{\partial r}^{n+1} = -\frac{\partial \overline{C}}{\partial r}^{n+1} \quad \text{on } r = 1, \tag{2.12}$$

$$\omega^{n+1} = 0,\ c^{n+1} = 0 \text{ at } r = r_\infty, \tag{2.13}$$

where the superscript n denotes the nth time level and F is given by

$$F = (\nabla \times \boldsymbol{u} \times \omega) \cdot \boldsymbol{e}^{(\phi)}.$$

These equations are solved using a Green's function method (Chang 1992) after they are Fourier transformed in the θ-direction and the entire system is upper triangular in θ-space. Each radial equation is solved in physical-r-space using Chebyshev collocation methods and back substitution yields the final solution.

For the cases studied, either 64 × 64 or 96 × 96 point grids are used with the stretch parameter set to values in the range $2 \leqslant L \leqslant 8$. The outer radius r_∞ was 250 at low Reynolds numbers ($Re < 1$) and 50 otherwise. Tests were made to verify accuracy of the resolution and to check that the value of r_∞ was sufficiently large. Typically a time step of $O(10^{-3})$ or smaller is used for the simulations. It was not uncommon to use a time step of $O(10^{-6})$ at the beginning and end of the acceleration periods owing to the discontinuous nature of the free-stream acceleration at these times.

2.2. *Validation*

Simulation results have previously (Part 1) been checked for accuracy against steady and oscillatory flows through comparison with previous numerical, experimental and theoretical results. In order to provide an initial test of the accuracy of our current simulations, we have compared our results with the Basset (1888) solution for unsteady Stokes flow. In this problem, the velocities are considered to be small and the accelerations large, so the convective acceleration term in the equations of motion may be neglected. Basset's estimate of the fluid force on sphere as the flow velocity accelerates from rest at a constant rate may be evaluated from (1.1), (1.2) and written in non-dimensional form as

$$C_{dB} = \frac{12}{Re} A_c t + 2A_c + 12A_c(2t/\pi Re)^{1/2}, \tag{2.14}$$

where Re is the flow Reynolds number at the end of the acceleration interval. A comparison of (2.14) with the present numerical simulations for the values of $A_c = 1.0$ and $Re = 0.1$ over the non-dimensional time interval $0 < t < 1$ shows that the relative difference while increasing over the interval is at most $O(10^{-4})$. Good agreement is also found with the higher-order results of Sano (1981) for the resultant force at low Reynolds numbers due to a flow started impulsively from rest, as is discussed later in this paper.

3. Linearly accelerating flow

In this section the flow structure and resulting fluid forces are examined for flows accelerating at a constant rate within the range $|A_c| \leqslant 2$ and $Re \leqslant 20$. An initially steady flow is accelerated at a constant rate between $t = t_s$ and $t = t_e$ at which point the acceleration is removed and the flow relaxes to a new steady flow regime. A very short time step is used to computationally resolve the transient behaviour near $t = t_s$ and $t = t_e$ where the acceleration changes rapidly. We begin by examining the flow structure for three different sets of simulations which illustrate many of the general features observed.

3.1. *Flow structure*

Typical streamfunction and vorticity contours for an accelerating flow are shown in figure 1 where the acceleration number $A_c = 1.0$ and the flow Reynolds number increases from 5 initially, to 10. The flow is from left to right in the figures. The coordinate $\theta = 0$ corresponds to the rear stagnation point along the sphere axis and $\theta = 180°$ is at the forward stagnation point. As the flow accelerates there is strong production of negative vorticity near the surface of the sphere, reinforcing the existing vorticity distribution, but this remains largely confined to a narrow region around the sphere. Advection of this enhanced surface vorticity is initially weak for this moderately strong acceleration, and it is only after the acceleration ceases that the vorticity diffuses away from the sphere and advection becomes more significant. Corresponding details of the surface pressure distribution and surface vorticity are shown in figure 2. The surface pressure $k(\theta)$ is measured relative to the pressure at the forward stagnation point,

$$k(\theta) = p(r = 1, \theta) - p(1, \pi). \tag{3.1}$$

As the flow accelerates there is a favourable pressure gradient at all points on the sphere. There is a dramatic change in the pressure distribution as the acceleration is removed, as may be seen by comparing the data for $t = t_e - \Delta t$ and $t = t_e + \Delta t$. This is associated with the added-mass effect discussed later. At time $(t_e + 1)$ the surface pressure has relaxed to a distribution closer to that of the new steady flow,

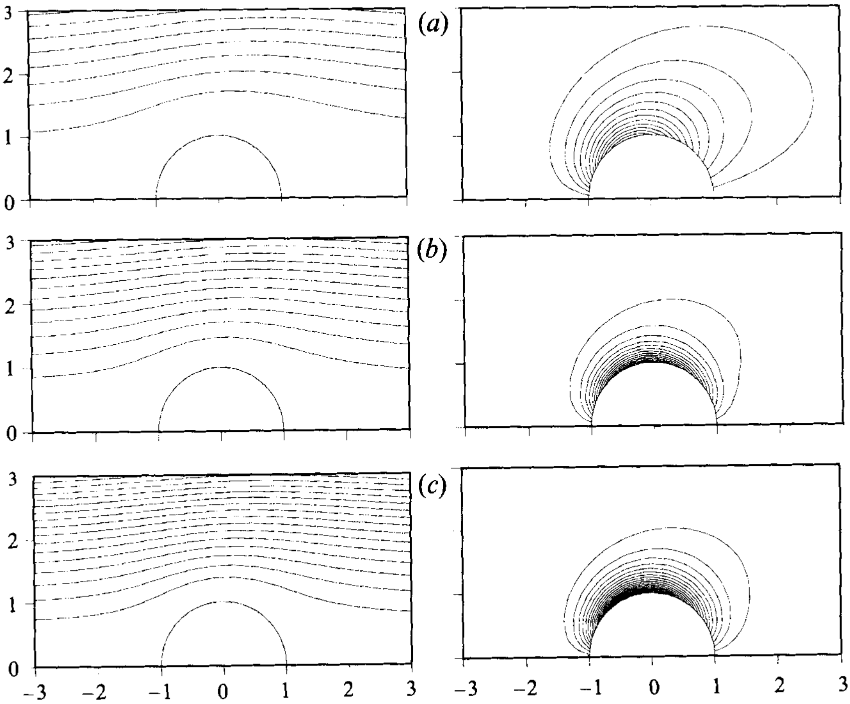

FIGURE 1. Streamlines (left column) and vorticity contours (right column) for a free stream accelerating from $U(t_s) = 0.5$ to $U(t_e) = 1$ with $Re = 10$ and $A_c = 1$; (*a*) $U(t) = 0.5$, (*b*) $U(t) = 0.75$, and (*c*) $U(t) = 1$.

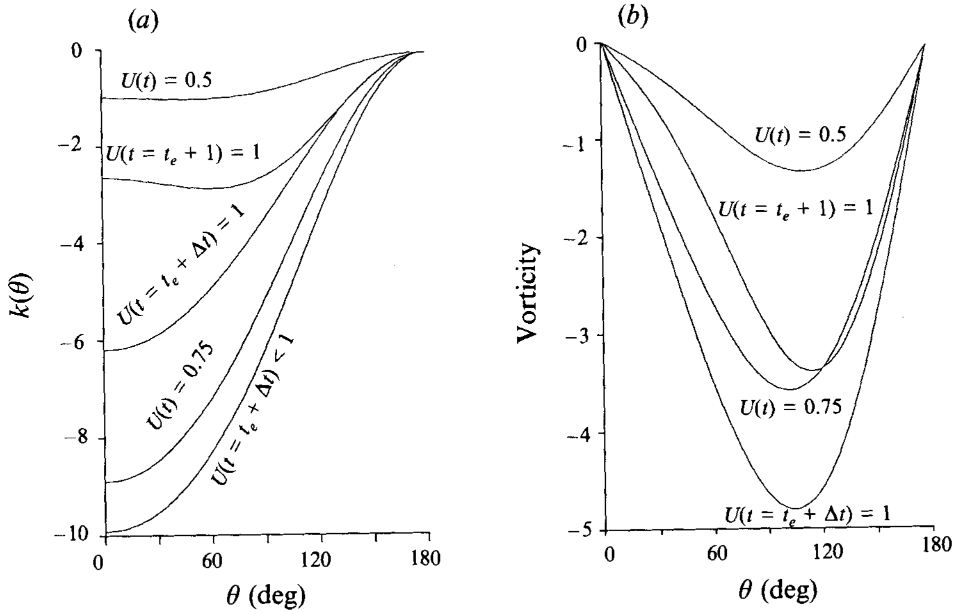

FIGURE 2. Surface pressure and vorticity distributions for a free stream accelerating from $U(t_s) = 0.5$ to $U(t_e) = 1$ with $Re = 10$ and $A_c = 1$; (*a*) surface pressure and (*b*) surface vorticity.

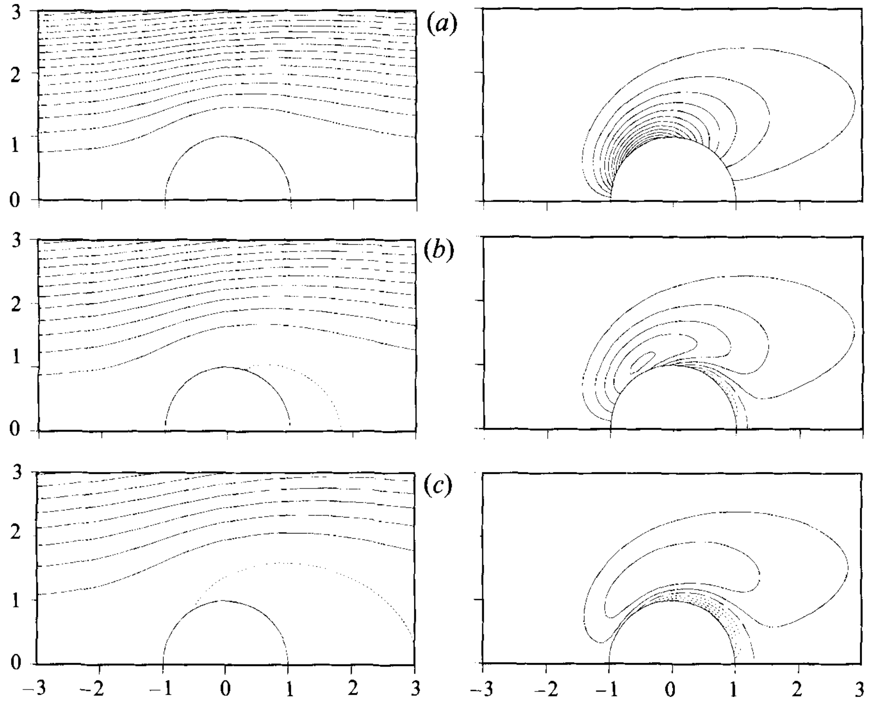

FIGURE 3. Streamlines (left column) and vorticity contours (right column) for a free stream deccelerating from $U(t_s) = 1$ to $U(t_e) = 0.5$ with $Re = 10$ and $A_c = -1$; (*a*) $U(t) = 1$, (*b*) $U(t) = 0.75$, and (c) $U(t) = 0.5$. Broken line shows the separation streamline (left). Vorticity contours are - - - -, positive; – –, zero; ——, negative.

with a mild adverse pressure gradient along the rear of the sphere, $0 < \theta < 90°$. The surface vorticity increases sharply during the acceleration: peak values are almost three times the initial steady-state value at the end of acceleration in cases where the instantaneous Reynolds number has doubled in value. The distribution also becomes nearly symmetric about the mid-plane at $\theta = 90°$ during acceleration, indicating the diminished effect of advection of vorticity. By time $(t_e + 1)$ the surface vorticity is close to that for steady flow; the peak value is within 3% of the final steady flow value reported in Part 1.

Streamline and vorticity contours for a decelerating flow with $A_c = -1$ and an initial Reynolds number $Re = 10$, which decreases to $Re = 5$, are shown in figure 3. For steady flows at these Reynolds numbers there is no separation but the streamlines show that quite quickly a separated flow region develops in response to the deceleration. The surface pressure and vorticity distribution are shown in figure 4. Soon after deceleration begins a strong adverse pressure gradient develops on the surface of the sphere. This is seen as a sharp change in $k(\theta)$ just after the deceleration begins, as shown by the data for $t = t_s$ and $t = t_s + \Delta t$, which is again associated with added-mass effects. Positive vorticity is generated on the rear portion of the sphere. This is confined to a region near the sphere surface which gradually extends further forward on the sphere. Further, the strength of the ambient negative vorticity associated with the initial steady flow becomes weaker.

Within the separated flow region, enclosed by the separation streamline, there is a recirculating flow which on the surface of the sphere is the reverse of that for steady flow conditions. The separation point on the sphere corresponds to the location of

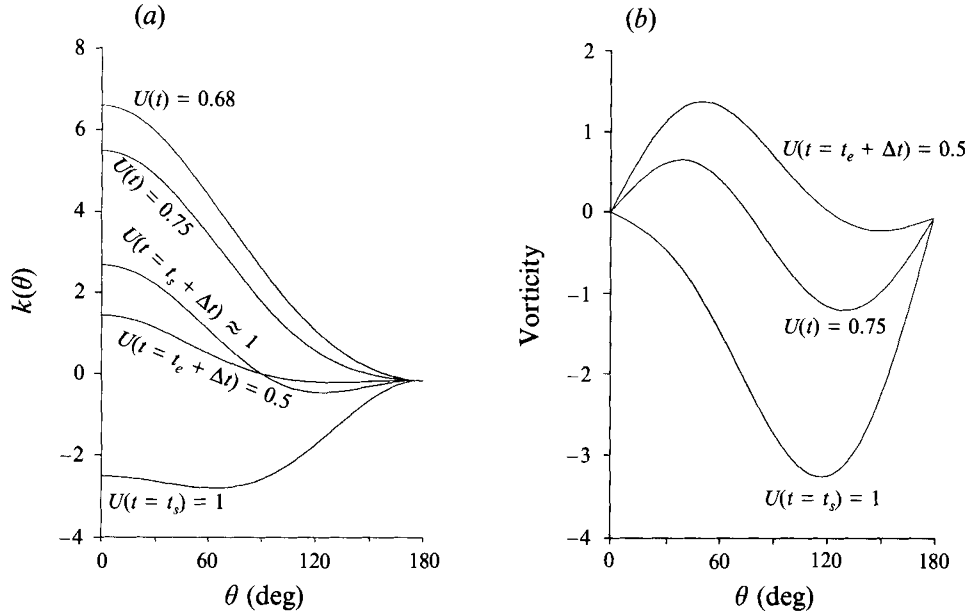

FIGURE 4. Surface pressure and vorticity distributions for a free stream decelerating from $U(t_s) = 1$ to $U(t_e) = 0.5$ with $Re = 10$ and $A_c = -1$; (*a*) surface pressure and (*b*) surface vorticity.

zero surface vorticity due to the no-slip boundary conditions (2.6). It is clear then from figure 3 that the positive vorticity is confined within the separated flow region, growing in extent as the region expands. This process may be characterized by two length scales: l, the length of the separation bubble given by the radial distance from the sphere surface at which the separation point streamline connects with the $\theta = 0$ axis, and δ, the thickness of the positive vorticity layer correspondingly defined as the radial distance from the sphere surface at which the zero vorticity contour connects with the $\theta = 0$ axis. Axial symmetry requires that $\omega = 0$ along the whole $\theta = 0$ axis; the zero vorticity contour is an envelope for the vorticity distribution. Table 1 shows different values of those length scales and the separation point angle θ_s for various rates of deceleration, at the instant when the deceleration is removed after an elapsed time Δt. These are compared with a Stokes diffusive length scale $\delta_s = (\nu \Delta t)^{1/2}$. For all the data in table 1 the final value of Re is half the initial value.

For other values of A_c and Re similar trends are observed distinguished mainly by whether the flow is accelerating or decelerating. For some of the decelerating flows investigated the separated flow region engulfs the sphere entirely, the ambient negative vorticity of the steady flow is completely detached from the sphere and the sphere is completely embedded in a region of positive vorticity. Examples of this are indicated in table 1. In the flows examined within this parameter range, we have found that if complete vorticity detachment occurs, this negative vorticity region is observed to eventually reconnect; these regions do not remain detached unless the final free-stream velocity, c_2, is zero in which case a standing eddy is formed to the side of the sphere.

As an illustration of how the flow vorticity returns to a steady state following a deceleration we include in figure 5 a sequence of vorticity contours for an initial $Re = 10$ and $A_c = -0.1$. The deceleration is relatively weak and at the end of the deceleration phase, shown in figure 5(*a*), the free-stream velocity is 0.1 *and*

Re	A_c	Δt	δ	δ_s	θ_s	l
0.1	−0.1	5.0	*	*	*	*
1	−0.1	5.0	*	*	*	*
5	−0.1	5.0	*	*	*	*
10	−0.1	5.0	0.12	1.0	0.622	0.518
15	−0.1	5.0	0.21	0.82	0.852	1.28
20	−0.1	5.0	0.25	0.71	0.931	1.84
0.1	−1	0.50	*	3.16	*	*
1	−1	0.50	0.12	1.0	0.932	0.40
5	−1	0.50	0.31	0.45	2.04	1.67
10	−1	0.50	0.30	0.32	2.20	2.07
15	−1	0.50	0.29	0.26	2.17	2.37
20	−1	0.50	0.28	0.22	2.20	2.61
0.1	−2	0.25	*	2.2	*	*
1	−2	0.25	0.28	0.71	2.93	1.13
5	−2	0.25	0.30	0.32	-	1.80
10	−2	0.25	0.28	0.22	-	2.14
15	−2	0.25	0.26	0.18	-	2.41
20	−2	0.25	0.25	0.16	-	2.64

TABLE 1. Length of positive vorticity region at rear of sphere δ, Stokes diffusive length scale $\delta_s = (\nu t)^{-1/2}$, angle of separation (in radians) θ_s, and length of recirculation region l at the end of deceleration period with $U(t_e) = 0.5$. A - denotes complete separation of the negative vorticity region. A * denotes no separation has occurred.

the associated Reynolds number is 1.0. In this instance the sphere is completely surrounded by a region of positive vorticity with the negative vorticity detached. Following the deceleration negative vorticity is again produced on the upstream side of the sphere, and the negative vorticity contours reattach to the surface here. The separation point moves back towards the rear stagnation point as the positive vorticity weakens. Eventually the negative vorticity in the free stream reconnects with the newly generated vorticity, but even after an elapsed non-dimensional time of 8 since the first frame the process is still not complete indicating that the return to the steady state is a slow process. The exact nature of the return to a steady state will be examined in further detail in the next section.

3.2. *Forces*

The forces acting on the sphere for $A_c = 1$ and $Re = 10$ are shown in figure 6. The resultant fluid force C_d, scaled as in (2.8), is the sum of the two components C_p and C_f due to the surface pressure distribution and viscous shear stresses respectively. A large jump in both C_d and C_p occurs at $t = t_s$, the time at which the acceleration period begins. Similarly, at the end of the acceleration period when $t \geqslant t_e$, there is a large drop in both C_d and C_p. The large change in the value of C_p is reflected in the sudden change in the surface pressure prior to and just after the end of the acceleration shown in figure 2. These differences should correspond to added-mass effects since changes due to viscous diffusion of vorticity and velocity-dependent history terms in such a short time period are negligible. Indeed the viscous shear stress component C_f exhibits no sharp changes either at the start or the end of the acceleration interval. The added-mass effect in an inviscid flow past a stationary sphere is strictly a pressure force proportional to the rate of acceleration of the free-stream velocity. The same is true for unsteady Stokes flow. There is an inertial component of value $\frac{4}{3}\mathrm{d}U/\mathrm{d}t$ to C_p due to the acceleration in the free stream $U(t)$. The inviscid added-mass contribution

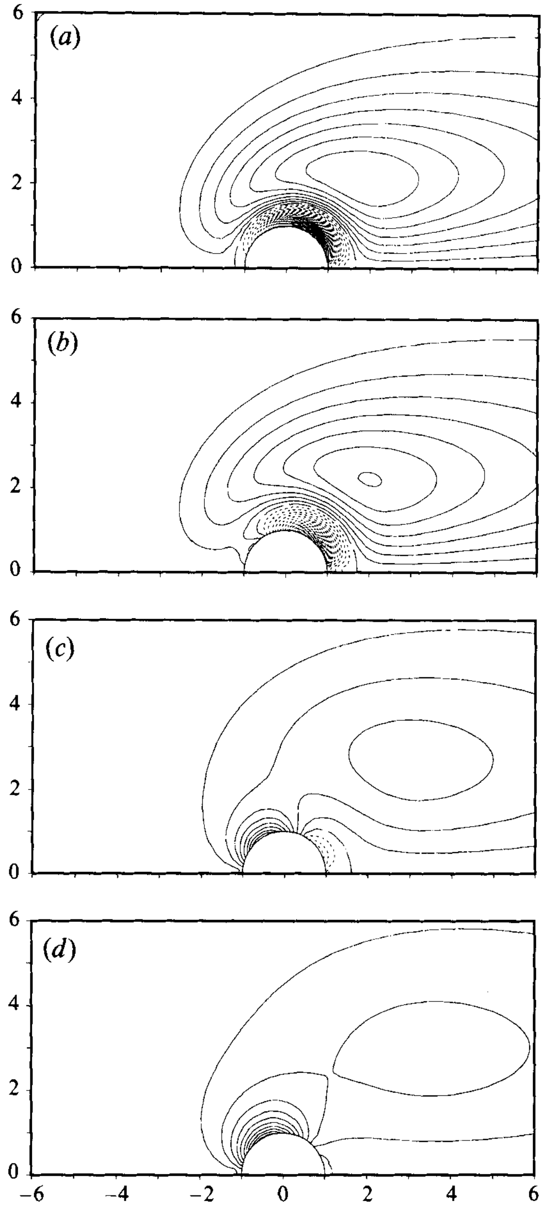

FIGURE 5. Vorticity contours of the flow following a deceleration, $A_c = -0.1$, from $Re = 10$ to 1.0 at various times after the deceleration ends at t_e; (*a*) $t = t_e$, (*b*) $t = t_e + 0.6$, (*c*) $t = t_e + 5.4$, (*d*) $t = t_e + 9.4$. Contours: - - - -, positive vorticity; – · –, zero vorticity; ——, negative vorticity.

is an additional $\frac{2}{3}\mathrm{d}U/\mathrm{d}t$ based on the usual estimate of an added-mass coefficient of $\frac{1}{2}$ as noted in (1.1). These combine to give a total inertial and added-mass contribution to C_p of

$$C_p^I = 2\frac{\mathrm{d}U}{\mathrm{d}t} = 2A_c. \tag{3.2}$$

Both at the start and the end of the acceleration interval, the observed change in pressure forces matches the expected value for the inviscid added-mass effect. The

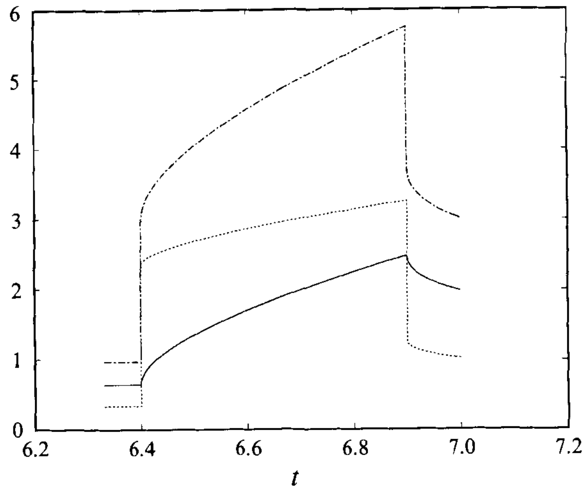

FIGURE 6. Drag force coefficients, C_f, C_p, and C_d *vs.* time during acceleration period for $Re = 10$, $A_c = 1$, $U(t_s) = 0.5$, $U(t_e) = 1$, $t_s = 6.4$ and $t_e = 6.9$; ———, C_f; - - - - -, C_p; — · —, C_d.

change in C_p at the start and at the end of acceleration, ΔC_{ps} and ΔC_{pe} respectively, seen in figure 6 agree with (3.2) to within 1% of C_p^I.

Rivero (1991) observed a similar large change in the fluid force C_d on a sphere at the start of a linearly accelerating flow. These simulations were made at initial Reynolds numbers of 0.1, 10 and 100 and positive accelerations $A_c = 0.001, 0.01, 0.1, 10$ and 100, taking account of the scaling used here. A similar procedure was used to separate the inertial component of the fluid force. In each case the change matched the estimate (3.2) though the separation of C_d into components C_f and C_p was not made.

We have extended our results to include both the start and the end of the acceleration and to include decelerating flows also. Table 2 shows values of ΔC_{ps}, the change in the pressure coefficient immediately (10^{-4} time unit) after acceleration has started, for different Reynolds and acceleration numbers. Corresponding changes ΔC_{pe} in C_p at the end of the acceleration period are also listed. The fluid forces for a decelerating flow with $A_c = -1$ and $Re = 10$ are shown in figure 7 and are similar in character to those for the accelerating case. The added-mass effect is apparent in the sudden changes in C_p; these too are reflected in the change in surface pressure shown in figure 4(*a*) prior to and just after the start of the deceleration. It is worth noting that ΔC_{pe} matches (3.2) even where flow separation has developed as a result of deceleration in the free stream. A comparison of tables 1 and 2 shows that for many of the decelerating flows listed a closed recirculating, separation bubble develops by the end of the deceleration interval, yet this has no apparent influence on ΔC_{pe}. This is an indication that the same will be true at higher Reynolds numbers where a separation bubble is a feature of steady flow.

In an inviscid irrotational flow, and in unsteady Stokes flow, the pressure distribution is solely responsible for the resultant added-mass force and is associated with a dipole potential for the flow. This gives rise to a surface pressure distribution, in dimensional form,

$$-\tfrac{1}{2}a\rho\cos\theta\frac{\mathrm{d}U}{\mathrm{d}t}$$

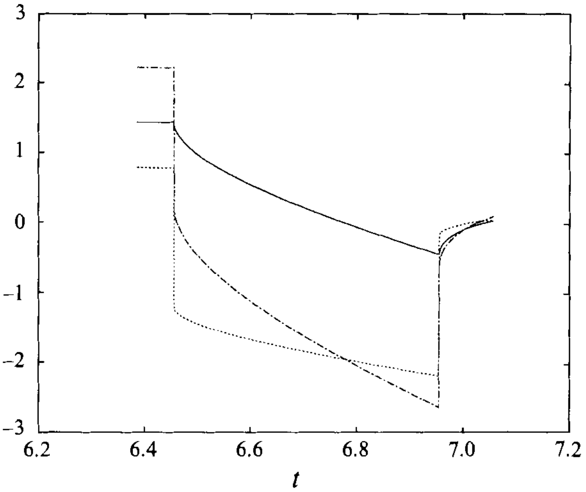

FIGURE 7. Drag force coefficients, C_f, C_p, and C_d *vs.* time during deceleration period for $Re = 10$, $A_c = -1$, $U(t_s) = 1$, $U(t_e) = 0.5$, $t_s = 6.455$ and $t_e = 6.955$; ——, C_f; - - - -, C_p; – · – · –, C_d.

and a component due to the free stream

$$-a\rho \cos\theta \frac{\mathrm{d}U}{\mathrm{d}t},$$

where $U(t)$ is the free-stream velocity. Non-dimensionally, the pressure coefficient associated with this added-mass force is given as

$$k(\theta) = \frac{p'(\theta)}{\frac{1}{2}\rho U_0^2} = -3A_c \cos\theta \tag{3.3}$$

where $p'(\theta)$ is the dimensional surface pressure.

In the present simulations the pressure is specified by a Fourier cosine series in θ as described in Part 1. To test whether or not the observed added-mass changes in C_p are associated with a corresponding dipole potential term we examine the first Fourier coefficient in the cosine series for the surface pressure. Figure 8(*a*) shows the first Fourier coefficient of the surface pressure $\hat{k}_1(t)$ for $A_c = 1.0$ and $Re = 10$. The jumps at t_s and t_e, $\Delta\hat{k}_1^s$ and $\Delta\hat{k}_1^e$ respectively, agree with (3.3). Similarly, the Fourier cosine coefficient $\hat{k}_1$ for the decelerating flow $A_c = -1$ and $Re = 10$, shown in figure 8(*b*), also has corresponding jumps which agree with (3.3) at t_s and t_e. Other values of $\Delta\hat{k}_1^s$ and $\Delta\hat{k}_1^e$ are given in table 2 for a range of accelerations and Reynolds numbers. None of the other Fourier coefficients that contribute to the drag force exhibit such a behaviour. Note that to avoid small, localized oscillations at t_e and t_s associated with the discontinuous acceleration, a very small but finite amount of time of $O(10^{-4})$ must be allowed to pass before exact values of C_p and $\hat{k}_1(t)$ can be obtained. This delay contributes to the slight discrepancy between the measured and the expected results.

It is significant to note that throughout these flow changes both the Fourier sine series in θ for the surface vorticity and the Fourier cosine series for the surface pressure are dominated by the first few terms in each series. No significant contribution comes from terms beyond the second harmonic. This is also a feature of the results of Dennis & Walker (1971) for steady flows past a sphere where spherical harmonics were used to represent the flow. There too at moderate to low Reynolds numbers

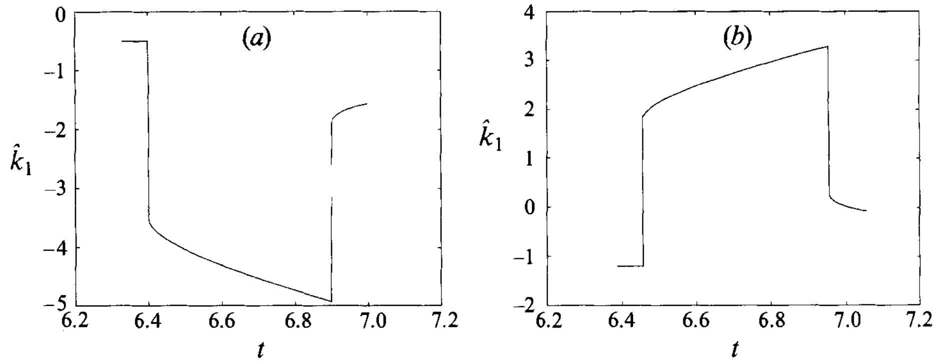

FIGURE 8. First Fourier coefficient of the surface pressure $\hat{k}_1$ *vs.* time during acceleration (deceleration) period for $Re = 10$; (*a*) $A_c = 1.0$, $U(t_s) = 0.5$, $U(t_e) = 1.0$, with $t_s = 6.4$ and $t_e = 6.9$; (*b*) $A_c = -1.0$, $U(t_s) = 1.0$, $U(t_e) = 0.5$ with $t_s = 6.455$ and $t_e = 6.955$.

Re	A_c	ΔC_{ps}	ΔC_{pe}	$\Delta\hat{k}_1^s$	$\Delta\hat{k}_1^e$
0.1	1	2.11	−2.11	−3.17	3.16
0.1	−1	2.11	2.10	3.17	−3.16
1	1	2.05	−2.05	−3.07	3.07
1	−1	−2.05	2.05	3.07	−3.07
10	1	2.02	−2.01	−3.01	3.02
10	−1	−2.02	2.01	3.02	−3.02
20	1	2.02	−2.02	−3.03	3.03
20	−1	−2.01	2.02	3.03	−3.03
0.1	2	4.22	−4.21	−6.33	6.32
0.1	−2	−4.22	4.21	6.33	−6.32
1	2	4.10	−4.09	−6.15	6.14
1	−2	−4.09	4.09	6.12	−6.14
10	2	4.07	−4.07	−6.12	6.10
10	−2	−4.08	4.08	6.12	−6.12
20	2	4.04	−4.04	−6.06	6.06
20	−2	−4.04	4.04	6.06	−6.06

TABLE 2. Change in pressure drag component at the beginning and end of acceleration period ΔC_{ps} and ΔC_{pe}, change in the first Fourier coefficient of the surface pressure coefficient at the beginning and end of acceleration period $\Delta\hat{k}_1^s$ and $\Delta\hat{k}_1^e$ for different Reynolds and acceleration numbers; $U(t_s) = 1$ and $U(t_e) = 0.5$ for $A_c = -1$ and -2; $U(t_s) = 0.5$ and $U(t_e) = 1$ for $A_c = 1$, and 2.

only the first few spherical harmonics contributed significantly to the surface vorticity distribution. This is an indication that the flow structure very close to the sphere is relatively simple. What is noteworthy is that this persists even for unsteady flow conditions where there is flow separation.

Beyond the added-mass effect certain other features of the forces during and after the acceleration are noteworthy. For accelerated motion both C_f and C_p, discounting the added-mass contribution, grow as the instantaneous Reynolds number increases. At the end of the acceleration period C_f is significantly higher than the eventual steady state value reached. For example, in the accelerated flow results of figure 6, $C_f = 2.46$ at the end of the acceleration period compared to its eventual steady-state value of 1.43. A significant amount of time (in this example, just over 4 time units) elapses before C_d reaches the new steady value, indicating a significant history effect

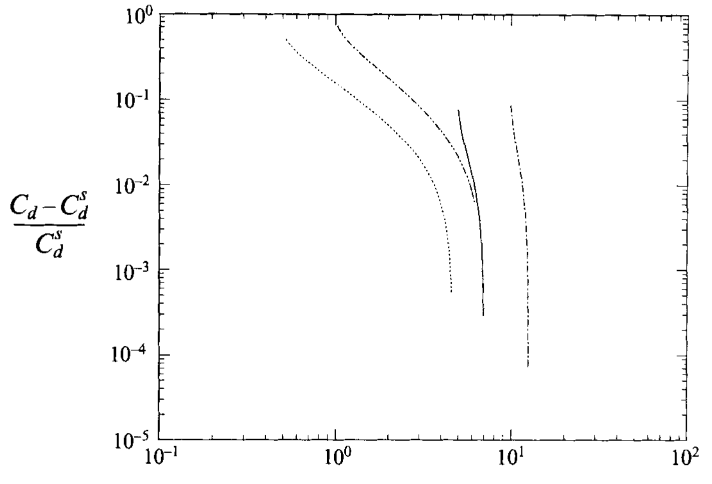

FIGURE 9. $(C_d - C_d^s)/C_d^s$ *vs.* time for $t > t_e$ at $Re = 10$, where C_d^s is the final steady-state drag force for $c_2 = 1$ following the acceleration: – ·· –, $c_1 = 0$ and $A_c = 1.0$; –·–, $c_1 = 0$ and $A_c = 0.1$; ·····, $c_1 = 0.5$ and $A_c = 1.0$; ———, $c_1 = 0.5$ and $A_c = 0.1$. Times are relative to $t_s = 0$

while the flow continues to adjust. For decelerated motion both C_f and C_p as well as the instantaneous Reynolds number decrease during the deceleration phase. In fact, as seen in figure 7 negative values of C_f may be attained even though the free-stream velocity remains positive. The force C_f is determined, as in (2.9), by the surface vorticity which is positive over an increasing portion of the sphere and is associated with the locally reversed flow on the sphere from the separation bubble. At the end of the deceleration, $t = t_e$, the value of C_f is below its final steady-state value. Figures 9 and 10 show how the drag forces approach steady-state values after after acceleration or deceleration has stopped for representative Reynolds numbers and acceleration numbers. Note that the drag forces continue to decay algebraically at large t when the free-stream velocity has decelerated to zero.

4. Impulsive motion

In order to further investigate the behaviour of the history drag force on a sphere we examine the special case where the free-stream velocity changes instantaneously from one constant value to another with an infinite acceleration. We allow only one change in velocity and both velocities are non-negative:

$$\left.\begin{aligned} U(t < 0) &= c_1, \\ U(t \geqslant 0) &= c_2, \\ 0 \leqslant c_1 \leqslant 1, 0 &\leqslant c_2 \leqslant 1. \end{aligned}\right\} \quad (4.1)$$

There are only two possible cases: an impulsive jump from a lower velocity c_1 to velocity $U = c_2 = 1$ or an impulsive drop from $U = c_1 = 1$ to a lower velocity c_2. When the free-stream velocity changes impulsively, an infinite inertial force is generated instantaneously. Following the step change the value of C_d eventually adjusts to the new steady-state value. In these results we focus on the short and intermediate term response during which C_d adjusts to within 0.5–1% of its final value. Care was taken here to ensure good spatial resolution and verify that r_∞ was

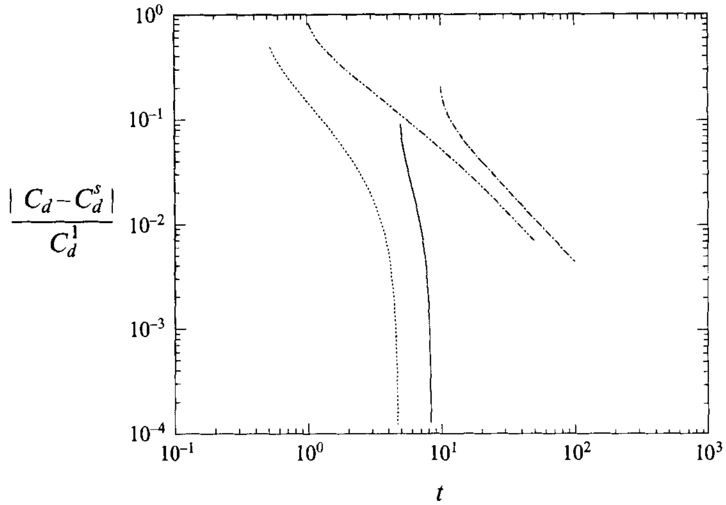

FIGURE 10. $|C_d - C_d^s|/C_d^1$ *vs.* time for $t > t_e$ at $Re = 10$, where C_d^s is the corresponding steady-state drag force following the deceleration and C_d^1 is initial drag force at $c_1 = 1$: ——, $c_2 = 0.5$ and $A_c = -0.1$; - - - -, $c_2 = 0.5$ and $A_c = -1.0$; – · –, $c_2 = 0$ and $A_c = -0.1$, – ·· –, $c_2 = 0$ and $A_c = -1.0$. Times are relative to $t_s = 0$.

large enough, since the zero-vorticity boundary condition there will eventually induce an exponential decay. For the cases where $Re > 1$ and $c_2 > 0$ the minimum value of r_∞ is 50, and the outer boundary condition should not be a factor till $t > 20$.

The first case considered is the equivalent of a sphere accelerating impulsively from rest to a constant velocity: $U(t < 0) = 0$, $U(t \geqslant 0) = 1$. Initial computational results for this problem have been given by Dennis & Walker (1972). Analytical solutions due to Sano (1981) and Lovalenti & Brady (1993*a*) to this problem for low Reynolds numbers indicate algebraic convergence of the drag force to the steady state proportional to $t^{-1/2}$ for t up to $O(Re)$ with a transition to algebraic convergence proportional to t^{-2} for $t = O(Re^{-2})$. Figure 11 shows current results for low and moderate Reynolds numbers as well as Sano's analytic solution. Here we have used the computed steady-state drag coefficients given in Part 1 as references for the computed results. Current results indicate an algebraic convergence slightly faster than the analytical $t^{-1/2}$ but which is valid for much larger t than suggested by the analytical solutions. This is followed by a more rapid algebraic convergence and then a final exponential decay at large times. Note too that this trend holds for moderate Reynolds numbers as well. Exponential convergence has been reported by Mei (1993) for the long term behaviour, though more recently Lawrence & Mei (1995) have obtained an approximate t^{-2} dependence in the final stage.

For a flow in which the free-stream velocity changes impulsively from one constant value to another (non-zero) value, the low Reynolds number results of Lovalenti & Brady (1993*a*,*b*) indicate exponential convergence for later times. Figure 12 shows how the computed drag force approaches the steady-state force after the free-stream velocity impulsively jumps from a velocity less than one to $U(t \geqslant 0) = 1$ for $Re = 0.1$ and $Re = 10$. These results are qualitatively similar to the impulsively started case with the drag force exhibiting an initial algebraic decay to the steady state slightly faster than $t^{-1/2}$ followed by a more rapid convergence at large t. That the behaviour for an impulsively started free stream and one in which the free stream changes from one constant velocity to another are similar in nature is somewhat surprising since

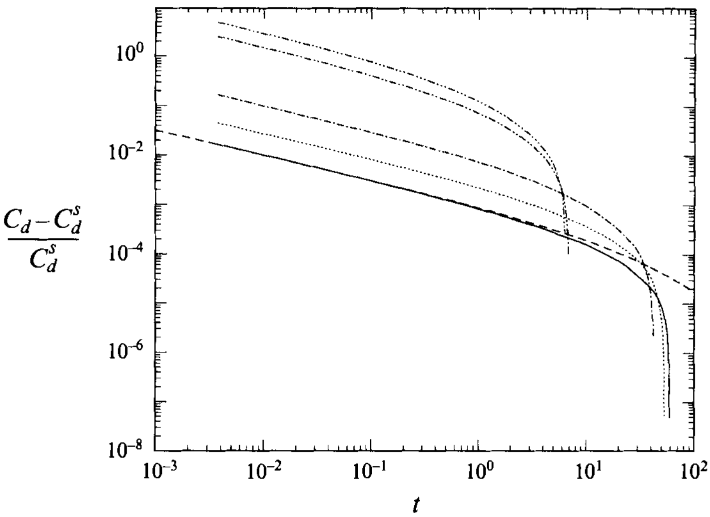

FIGURE 11. $(C_d - C_d^s)/C_d^s$ *vs.* time for an impulsively started free stream velocity where C_d^s is the final steady-state drag force at $U = c_2 = 1$: ——, $Re = 0.1$; - - - - - , $Re = 0.2$; – · – ·, $Re = 0.5$; – ·· – ··, $Re = 5$; – · · · –, $Re = 10$. Sano's analytical result scaled by the long term asymptotic values of this solution is shown, – –.

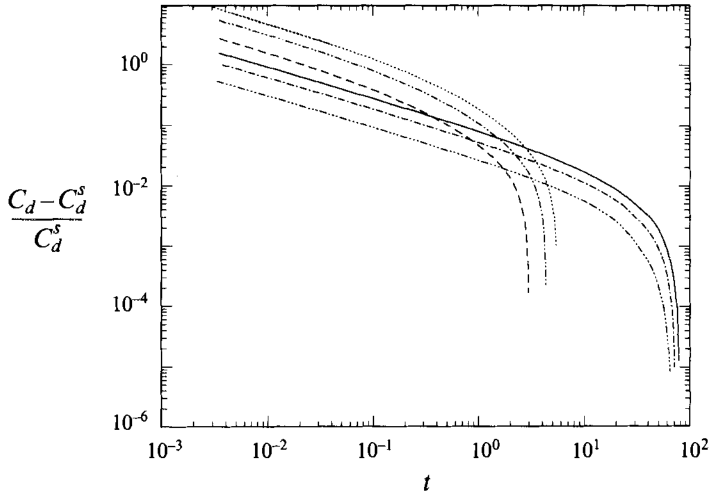

FIGURE 12. $(C_d - C_d^s)/C_d^s$ *vs.* time for a free-stream velocity impulsively raised from $U = c_1$ to $U = c_2 = 1$: ——, $c_1 = 0.25$ and $Re = 0.1$; - - - -, $c_1 = 0.25$ and $Re = 10$; – · –, $c_1 = 0.5$ and $Re = 0.1$; – ·· –, $c_1 = 0.5$ and $Re = 10$; – · · · –, $c_1 = 0.75$ and $Re = 0.1$; – – –, $c_1 = 0.75$ and $Re = 10$.

it is expected that the impulsively started case would take much longer to converge owing to the necessity for the wake region to both form and develop fully.

An impulsively stopped free stream with $U(t < 0) = 1$ and $U(t \geqslant 0) = 0$ is much different than the impulsively started flow. Here, after the free stream is stopped, a large eddy is formed to the side of the sphere (figure 13) generating a negative drag force which decays in time as the fluid viscosity weakens the eddy through diffusion. Since the drag force is negative, how the absolute value of the drag force approaches zero is of interest. Figure 14 shows the behaviour of the drag force for different initial Reynolds numbers. As in the impulsively started case, the drag force

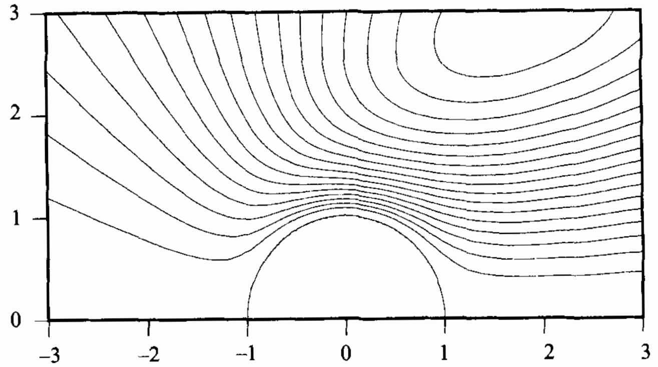

FIGURE 13. *Streamlines at* $t_s + 0.005$ *just after the free-stream velocity has been impulsively brought to rest, initially* $Re = 10$.

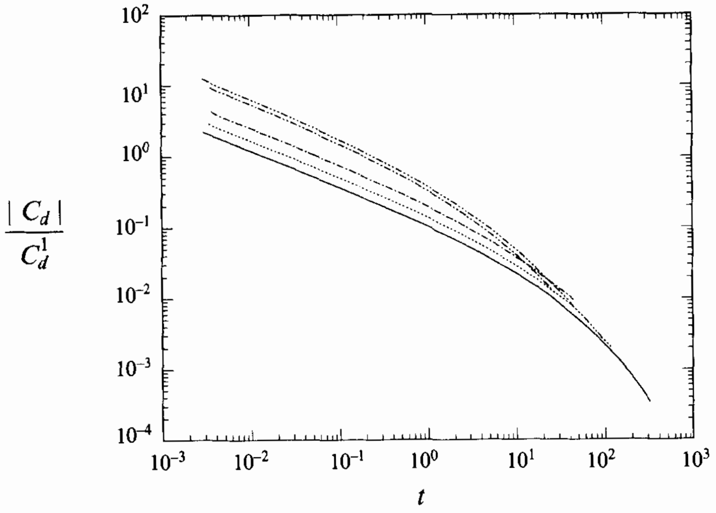

FIGURE 14. $|C_d|/C_d^1$ *vs.* time for an impulsively stopped free-stream velocity, C_d^1 is the corresponding initial drag force at $c_1 = 1$, the initial Reynolds numbers are : ——, $Re = 0.1$; · · · · ·, $Re = 0.2$; – · –, $Re = 0.5$; – ·· –, $Re = 5$; – · · · –, $Re = 10$.

initially decays at an algebraic rate slightly greater than $t^{-1/2}$. However, this decay rate remains algebraic for large t; there is no evidence of exponential convergence for the impulsively stopped flow. This is a clear indication that impulsively started and stopped free streams yield different behaviour in these time intervals and that the destruction of the wake region strictly through diffusion is a much slower process than the construction of the wake region through convection and diffusion even in the low Reynolds number flow regime.

Finally, figure 15 shows the computed drag forces for a sphere in which the free stream velocity impulsively drops to another non-zero value. As before, the convergence is initially algebraic followed finally by a rapid exponential convergence. In contrast to the previous example the free-stream velocity has been reduced here but not eliminated so that the existing wake structure is weakened but not completely dissipated. Both convection of vorticity by the flow and viscous diffusion continue to contribute to this process.

Accurately determining the final long term relaxation of the drag force to the

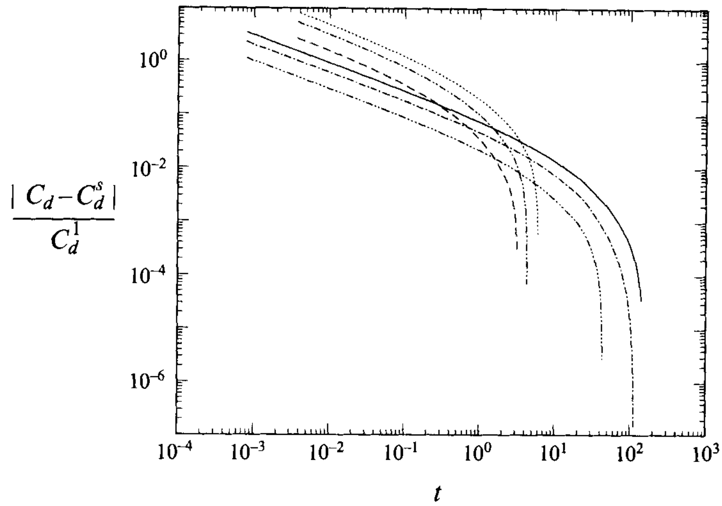

FIGURE 15. $|C_d - C_d^s|/C_d^1$ *vs.* time for a free-stream velocity impulsively reduced from an initial $c_1 = 1$, with corresponding drag force C_d^1, to a lower value c_2 with a final steady-state drag force C_d^s; initial *Re* and c_2 are : ——, $Re = 0.1$ and $c_2 = 0.25$; – · –, $Re = 0.1$ and $c_2 = 0.5$; – · · · –, $Re = 0.1$ and $c_2 = 0.75$; · · · · ·, $Re = 10$ and $c_2 = 0.25$; – ·· –, $Re = 10$ and $c_2 = 0.5$; – – –, $Re = 10$ and $c_2 = 0.75$.

steady-state value is very difficult. The present results indicate an initial power law response and then a somewhat faster than algebraic decay during which the force adjusts to within 0.5–1% of its final value. Except for the impulsively stopped sphere there is no discernible 'second power law' before an exponential cut-off is reached. Beyond the influence of the outer boundary already mentioned the results in the final stage are sensitive to errors in determining C_d^s, used as the asymptotic reference value, and the accuracy-order of the time-stepping algorithm used in these long-term calculations. Here the scheme is second-order accurate, the minimum acceptable. Even allowing for possible influences of the outer boundary conditions, the results of figures 9 and 10 for accelerating and decelerating flows strongly suggest a faster than algebraic/exponential final relaxation to steady state in flows involving a change between non-zero velocities. The results also show that the viscous relaxation process does not persist indefinitely. One of the difficulties in calculating particle trajectories in a flow where a history term is included is the need to retain a long record of the particle acceleration relative to the surrounding fluid. There appears to be an effective finite cut-off to this process in many cases.

5. Discussion

Linearly accelerating and decelerating flow past a rigid sphere has been investigated numerically. In the accelerating flow case the surface-generated vorticity is confined to a region near the sphere at high acceleration numbers. At low acceleration numbers the vorticity is free to convect downstream of the sphere. In the decelerating flow, owing to the generation of an adverse pressure gradient, separation is observed at Reynolds numbers well below those at which separation occurs in a steady flow. In some cases, the flow completely detaches from the sphere with an inner reverse flow completely engulfing the sphere. Although the negative vorticity associated with the initial flow is free to convect downstream, in all cases studied this region reattaches to the sphere after the deceleration period ends. At higher acceleration numbers the thickness of the positive, surface-generated vorticity layer created within the recirculation region matches the Stokes diffusion length δ_s. However, this is not the case at low Reynolds or acceleration numbers.

Negative viscous and pressure forces on the sphere are observed during the deceleration period meaning that instead of retarding the flow, the drag forces act to maintain it even though the flow has not changed direction. In both the accelerating and decelerating flows the pressure component of the force exhibits behaviour that is well described by an inviscid added-mass effect. This result is confirmed through examination of the surface pressure component associated with this force and the structure of this surface distribution. Historically there has been much discussion, see for example Torobin & Gauvin (1959), as to whether added-mass is an appropriate concept outside of the context of potential flows especially where viscous, finite Reynolds number effects play a strong role. There has been much discussion too on how to define added-mass in general. For unsteady motion in the low Reynolds number Stokes regime the concept has a clear meaning, though the added-mass force will depend on the spatial variations in the underlying flow (Maxey & Riley 1983). The results here, at least for these Reynolds numbers, show that added-mass has a very clear significance and interpretation based on the pressure forces in the flow.

The present data on the relaxation of the drag force to the steady state after acceleration were found to be insufficient to determine the exact nature of the history drag force. However, from the results for the impulsively changed free-stream velocity, we found that the Basset decay rate of $t^{-1/2}$ is adequate in approximating the initial behaviour of the history drag forces with changes in the decay rate only occurring once the drag force was within a few percent of the final steady-state value. We have found that at later times, the convergence is more rapid and finally exponential for all but a sphere brought to rest, in which case the convergence was found to remain algebraic. This suggests that the effects of vorticity convection by the flow act to give a rapid convergence in the long time limit, even without the prior existence of a wake region.

Support for this work was provided by a DARPA URI Award (ONR-N00014-86-K075) and by the Fluid Dynamics Program of the Office of Naval Research (ONR-N00014-91-J1340). Computing resources were provided by the Pittsburgh Supercomputing Center.

REFERENCES

Bassett, A. B. 1888 *A Treatise in Hydrodynamics*, Vol. II. Cambridge: Deighton, Bell, and Co.

Batchelor, G. K. 1967 *An Introduction to Fluid Dynamics*. Cambridge University Press.

Bentwich, M. & Miloh, T. 1978 The unsteady matched Stokes-Oseen solution for the flow past a sphere. *J. Fluid Mech.* **88**, 17–32.

Chang, E. J. 1992 Accelerated motion of rigid spheres in unsteady flow at low to moderate Reynolds numbers. PhD thesis, Brown University.

Chang, E. J. & Maxey, M. R. 1994 Accelerated motion of rigid spheres in unsteady flow at low to moderate Reynolds numbers. Part 1. Oscillatory motion. *J. Fluid Mech.* **277**, 347–379.

Dennis, S. C. R. & Walker, J. D. A. 1971 Calculation of the steady flow past a sphere at low and moderate Reynolds numbers. *J. Fluid Mech.* **48**, 771–789.

Dennis, S. C. R. & Walker, J. D. A. 1972 Numerical solutions for time-dependent flow past an impulsively started sphere. *Phys. Fluids* **15**, 517–525.

Lawrence, C. J. & Mei, R. 1995 Long-time behaviour of the drag on a body in implusive motion. *J. Fluid Mech.* **283**, 307–327.

Lovalenti, P. M. & Brady, J. F. 1993*a* The hydrodynamic force on a rigid particle undergoing arbitrary time-dependent motion at small Reynolds umber. *J. Fluid Mech.* **256**, 561–605.

Lovalenti, P. M. & Brady, J. F. 1993*b* The force on a sphere in a uniform flow with small-amplitude oscillations at finite Reynolds number. *J. Fluid Mech.* **256**, 607–614.

Marcus, P. S. & Tuckerman, L. S. 1987 Simulation of flow between concentric rotating spheres. Part 1. Steady states. *J. Fluid Mech.* **185**, 1–30.

Maxey, M. R. & Riley, J. J. 1983 Equation of motion for a small rigid sphere in a nonuniform flow. *Phys. Fluids* **26**, 863–889.

Mei, R. 1993 History force on a sphere due to a step change in the free-stream velocity. *Intl J. Multiphase Flow* **19**, 509–525.

Mei, R. & Adrian, R. J. 1992 Flow past a sphere with an oscillation in the free-stream velocity and unsteady drag at finite Reynolds number. *J. Fluid Mech.* **237**, 323–341.

Mei, R., Lawrence, C. J., & Adrian, R. J. 1991 Drag on a sphere with fluctuations in the free stream velocity. *J. Fluid Mech.* **233**, 613–631.

Orszag, S. A. 1974 Fourier series on spheres. *Mon. Weather Rev.* **102**, 56–75.

Rivero, M. 1991 Etude par simulation numererique des forces exercées sur une inclusion sphérique par un écoulement accéléré. Thése de Doctorat, INPT.

Rivero, M., Magnaudet, J. & Fabre, J. 1991 Quelques résultants nouveaux concernant les forces exercées sur une inclusion sphérique par en écoulement accéléré. *C.R. Acad. Sci. Paris* **312**(II), 1499–1506.

Sano, T. 1981 Unsteady flow past a sphere at low Reynolds number. *J. Fluid Mech.* **112**, 433–441.

Torobin, L. B. & Gauvin, W. H. 1959 Fundamental aspects of solids-gas flow. Part III. Accelerated motion of a particle in a fluid. *Can. J. Chem. Engng* **38**, 224–236.